PAPER

Check for updates

Facile synthesis of BiSI and $Bi_{13}S_{18}I_2$ as stable electrode materials for supercapacitor applications†

Huapeng Sun,[a] Guiling Yang,[b] Jie Chen,[a] Caroline Kirk*[a] and Neil Robertson (ID) *[a]

In this paper, we demonstrate a novel synthetic route of two bismuth chalcogenide materials 3-D hexagonal $Bi_{13}S_{18}I_2$ and 3-D orthorhombic BiSI, and investigate their potential as the active electrode material for supercapacitors. Both pure BiSI and $Bi_{13}S_{18}I_2$ powders were obtained for the first time at relatively low temperature (120 °C) in a solution system. We studied the effects of different reaction conditions on the surface morphology of the product and found that at a relatively low temperature of 120 °C under atmospheric pressure, the materials can yield smaller crystallite size and higher specific surface area, further increasing the capacitance compared to the synthesis under hydrothermal conditions. Cyclic voltammetry and galvanostatic charge–discharge measurements of the materials were studied using three-electrode and two-electrode configurations at a variety of currents. The galvanostatic charge–discharge measurement results show that the $Bi_{13}S_{18}I_2$ electrode has a maximum areal capacitance of 247 mF cm^{-2} at the current density of 5 mA cm^{-2} and excellent capacitance retention of 98.4% after 5000 cycles at the current density of 50 mA cm^{-2} in 3.0 M KOH electrolyte as a two-electrode electrical double-layer capacitor system (EDLC). The BiSI and $Bi_{13}S_{18}I_2$ powders have been characterized through PXRD, XPS, Raman spectroscopy, TGA–DSC, BET, SEM and TEM. This facile route to the synthesis of both $Bi_{13}S_{18}I_2$ and BiSI with superior stability has promising potential for low-cost and effective electrochemical supercapacitor applications.

Introduction

In recent years, the demand for efficient, economical and environmentally-friendly energy storage systems for electronics, electric vehicles and smart sustainable energy grid applications has grown dramatically, and the design and development of sustainable energy storage devices has become an important research area.[1–3] Supercapacitors and batteries are the most widely used in electronic devices and electric vehicles, in terms of the available different types of electrochemical energy storage devices. Traditionally, supercapacitors have been considered as power supplies with high power capability but low energy density when compared with batteries.[4–6] Much effort has been put into improving the energy density of supercapacitors, in which asymmetric hybrid systems have been extensively studied by combining faradaic-type rechargeable battery electrodes with double-layer charge storage carbon electrodes.[7–10] Bi-Based

materials are considered as potential candidates for supercapacitors due to the low toxicity, high electrochemical stability, high redox reversibility and relatively high power. Specifically, Bi_2O_3 and Bi_2S_3 have been shown to have promise in supercapacitors and electrochemical devices.[11–16] Bi_2S_3 is known to exhibit a very diverse range of crystal forms, including nanorods and nanoribbons that can be tuned to enhance the performance of the active electrode material in supercapacitors, generally in a pseudocapacitor mode.[17–20] Among the common Bi-based chalcogenides, BiSI has been studied as a potential photovoltaic material due to its n-type semiconductor properties and high absorption coefficient. However, the possibility of BiSI in capacitor applications has not been studied. In addition, the manufacture of bismuth chalcogenides typically requires high annealing temperatures and a multi-step procedure, which makes economic feasibility very low. For example, synthesis of BiSI required a Pyrex tube which was flame-sealed under vacuum while in an ice bath to prevent loss of I_2 vapor or to be heated to 900 K.[21–26] Recently, a solvothermal synthesis route was reported, however this still requires sealed and pressure conditions.[27]

To the best of our knowledge, a simple one-step, moderate-temperature solution synthesis route has not been reported.

[a] *School of Chemistry and EaStCHEM, University of Edinburgh, King's Buildings, David Brewster Road, Edinburgh, Scotland EH9 3FJ, UK.*
E-mail: Caroline.Kirk@ed.ac.uk, Neil.Robertson@ed.ac.uk

[b] *Hebei North university, Zhangjiakou 075000, Hebei, P. R. China*

† Electronic supplementary information (ESI) available. See DOI: 10.1039/d0tc02993a

This journal is © The Royal Society of Chemistry 2020

J. Mater. Chem. C, 2020, 8, 13253–13262 | 13253

In this paper, we report the controlled synthesis of two different bismuth chalcogenide materials, BiSI and $Bi_{13}S_{18}I_2$, from solution in a single and facile step. Their electrochemical performance as electrode materials for supercapacitors was tested in 3.0 M KOH electrolyte, using both a three-electrode system and a two-electrode electrical double-layer capacitor (EDLC) system. Improved supercapacitor performances were shown by the materials prepared in an open beaker under mild conditions (BiSI-*b*, $Bi_{13}S_{18}I_2$-*b*) compared with control samples prepared in an autoclave (BiSI-*a*, $Bi_{13}S_{18}I_2$-*a*). Operating as a pseudocapacitor, the BiSI-*b* electrode shows the highest specific capacitance of 128 F g^{-1} among four prepared electrodes at a current density of 2.0 A g^{-1} and excellent capacitance retention of 78.5% over 2000 cycles at a current density of 10.0 A g^{-1} in a three-electrode system. The $Bi_{13}S_{18}I_2$-*b* electrode as the active material in EDLC-type supercapacitors achieved a superior cycle stability with 98.4% capacitance retention after 5000 cycles at a current density of 50 mA cm^{-2} and a highest areal capacitance of 247 mF cm^{-2} at a current density of 5 mA cm^{-2}. This is more than 4 times higher compared with our previously reported thin-film $Bi_{13}S_{18}I_2$ electrode[28] (53.65 mF cm^{-2} at 2 mA cm^{-2}).

Results and discussion

The two bismuth chalcogenide iodide materials, labelled BiSI-*b* and $Bi_{13}S_{18}I_2$-*b*, were prepared by a novel one step synthesis route at relatively low temperatures in an open beaker, as described in the Experimental section. For comparison we will also present results from the same materials synthesized using an autoclave at 160 °C, and labelled BiSI-*a* and $Bi_{13}S_{18}I_2$-*a*. Fig. 1A shows PXRD patterns of the as-prepared materials BiSI-*a* and BiSI-*b* and confirms both samples contain BiSI. Refinement of the PXRD data using a least squares refinement procedure was carried out in space group Pnam. The refined unit cell parameters for BiSI-*a* are a = 8.501(3) Å, b = 10.244(4) Å and c = 4.172(2) Å and for BiSi-*b*, a = 8.497(2) Å, b = 10.243(3) Å and c = 4.171(2) Å. These are in in good agreement with standard literature values (a = 8.5138 Å, b = 10.2639 Å and c = 4.1742 Å), (ICDD PDF card no. 43-652).[29] The samples generally showed very good phase purity, although for the BiSI-*a* sample, weak diffraction peaks at 15.7°, 23.7°, 24.9° and 28.6° were also observed, which can be matched to the presence of Bi_2S_3 as a minor impurity phase.

Comparison of the PXRD patterns of the $Bi_{13}S_{18}I_2$-*a* and $Bi_{13}S_{18}I_2$-*b* to a standard pattern are shown in Fig. 1B. Both datasets were refined using a least squares refinement procedure in the primitive trigonal space group $P3$, with the refined unit cell parameters for $Bi_{13}S_{18}I_2$-*a*: a = 15.634(6) Å, and c = 4.014(2) Å, and for $Bi_{13}S_{18}I_2$-*b*: a = 15.63(2) Å, and c = 4.011(3) Å. The refined values are in good agreement with values published by Groom *et al.* (a = 15.612 Å, and c = 4.0168 Å, ICSD collection number 243730).[21] The PXRD pattern collected on $Bi_{13}S_{18}I_2$-*a* had the presence of weak impurity peaks at 15.7°, 22.4° and 25.2° 2θ, which could be attributed to the presence of Bi_2S_3. $Bi_{13}S_{18}I_2$ has been previously reported as having the formula
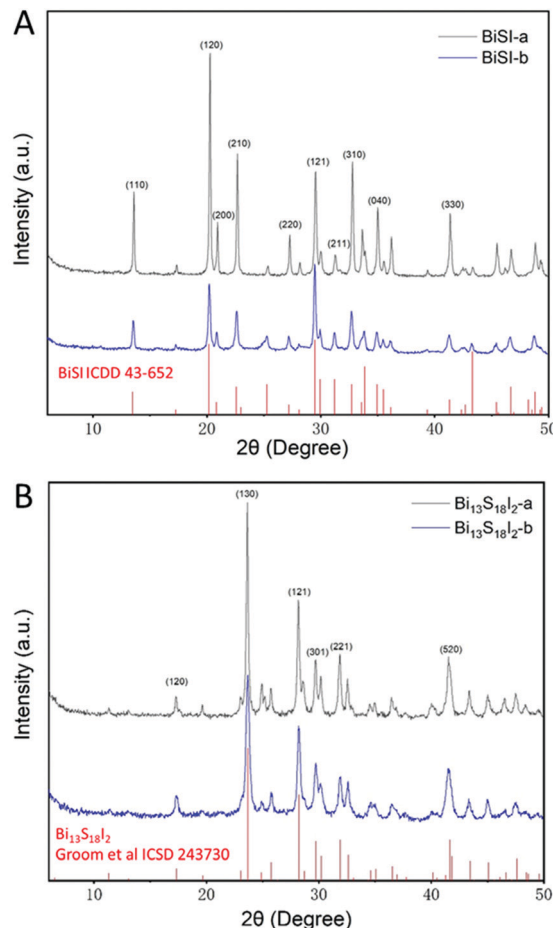

Fig. 1 PXRD patterns of the as-prepared BiSI powder (A) and $Bi_{13}S_{18}I_2$ powder (B).

$[Bi(Bi_2S_3)_9I_3]_{2/3}$,[30] $Bi_{19}S_{27}I_3$[26] and $Bi_{13}S_{18}I_2$[25] we adopted the formula $Bi_{13}S_{18}I_2$[21] which contains $[Bi_2]^{4+}$ dimers and its unit cell is shown in Fig. S1 (ESI†).

We also analyzed the products from syntheses of the BiSI material carried out at different temperatures, 60 °C, 90 °C, 120 °C and 150 °C, using PXRD and the data are presented in Fig. S1 (ESI†). This shows that at a lower synthesis temperature of 60 °C, Bi^{3+} ions react directly with I$^-$ and oxygen in the air, forming BiOI rather than BiSI. As the temperature rises, Bi^{3+} starts to react with thioacetamide to form BiSI; at 90 °C the product is a mixture of BiOI and BiSI. When the reaction temperature is too high, reaching 150 °C, the decomposition of thioacetamide is too fast, and only Bi_2S_3 is formed. Only controlling the temperature at 120 °C for 1 hour was found to form pure BiSI without the presence of BiOI or Bi_2S_3. The suggested synthesis route is:
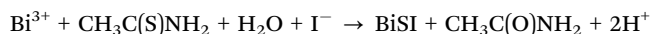
$$Bi^{3+} + CH_3C(S)NH_2 + H_2O + I^- \rightarrow BiSI + CH_3C(O)NH_2 + 2H^+$$

Fig. 2 shows SEM images of BiSI and $Bi_{13}S_{18}I_2$ samples, with both having needle-like morphologies. BiSI-*a* presents as bundles of needles, with each needle having a length of 10 to 30 μm, whereas for BiSI-*b*, the needles are dispersed, and each needle
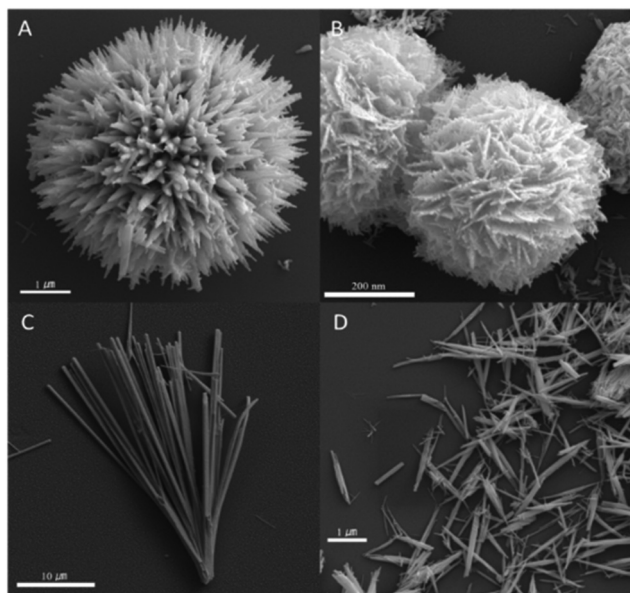
13254 | *J. Mater. Chem. C*, 2020, **8**, 13253–13262

This journal is © The Royal Society of Chemistry 2020

Fig. 2 SEM micrographs of, $Bi_{13}S_{18}I_2$-*a* (A) and $Bi_{13}S_{18}I_2$-*b* (B) BiSI-*a* (C), BiSI-*b* (D).
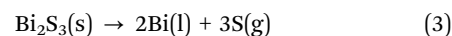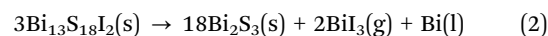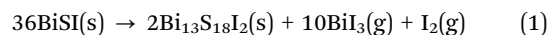
has a length of about 1 to 2 μm, much smaller than the length of the BiSI-*a* needles. As shown in Fig. 2A, the morphology of $Bi_{13}S_{18}I_2$-*a* can be described as flower-like, formed by needle-like branches, each of which has a length of about 1 to 2 μm. This significantly increases the specific surface area when compared to the BiSI samples. A flower-like microstructure is reported to allow the construction of high performance electrodes because of the significant connection between the crystallites, which will facilitate the conduction of charge in the active material layer.[31] $Bi_{13}S_{18}I_2$-*b* also shows a flower-like morphology similar to $Bi_{13}S_{18}I_2$-*a*, not formed by needles, but instead through interconnection of sheet-like nanoparticles of around 60 nm length. This special three-dimensional flower shape not only increases the specific surface area, but also improves the performance as supercapacitor (*vide infra*); the interstitial spaces between the nanoparticles in the structure can provide more channels for electrolyte ions to access and more electroactive sites, while the sheet structure formed by the nanorods can reduce the internal resistance.[32]

TEM was used to study the morphology of BiSI-*b* and $Bi_{13}S_{18}I_2$-*b* in more detail, (Fig. 3). It can be clearly seen that BiSI-*b* has a single needle like morphology with a length of around 550 nm. The high resolution TEM image presented in Fig. 3B of BiSI-*b* clearly shows two different sets of lattice fringes, with measured interplanar spacings of 0.30 nm, corresponding to the (121) crystallographic plane of BiSI, and 0.44 nm, corresponding to the (120) crystallographic plane. These are two of the most intense reflections observed by PXRD (Fig. 1). The corresponding selected-area electron diffraction (SAED) patterns of BiSI-*b* (inset in Fig. 3B) shows that the BiSI-*b* sample has a 3-D orthorhombic structure. It can be seen from Fig. 3D that the sheet-like structure of $Bi_{13}S_{18}I_2$-*b* is formed by nanorod with a length from 50 nm to 120 nm. The high

resolution TEM image of $Bi_{13}S_{18}I_2$-*b*, presented in Fig. 3F, shows a single crystallographic plane (130) with a measured interplanar spacing of 0.375 nm, consistent with the most intense reflection observed by PXRD (Fig. 1). The corresponding SAED pattern (inset in Fig. 3E) shows a 3-D hexagonal structure indicated good crystallinity. The corresponding Bi, S and I elemental maps in Fig. 3G and H, show the three elements are very uniform, further demonstrating the homogeneous growth of pure BiSI and $Bi_{13}S_{18}I_2$ crystals during synthesis instead of a mixture of different materials containing these elements in different proportions.

Raman spectra were collected on several samples of BiSI-*b* and $Bi_{13}S_{18}I_2$-*b* over the wavenumber range 60–500 cm^{-1} and sample datasets are shown in Fig. 4. Both BiSI-*b* and $Bi_{13}S_{18}I_2$-*b* show low energy Bi–S vibrational modes at 220 cm^{-1} and 280 cm^{-1}, which are similar to Bi_2S_3.[33] Kalpen *et al.* reported that a Bi–Bi stretching mode can be observed between 102 and 108 cm^{-1} due to the presence of Bi_2^{4+} dimers.[33] A strong peak is observed at 106 cm^{-1} in the spectrum of $Bi_{13}S_{18}I_2$-*b*, confirming the presence of Bi_2^{4+} dimers in this structure. The comparison of BiSI-*a*, BiSI-*b*, $Bi_{13}S_{18}I_2$-*a* and $Bi_{13}S_{18}I_2$-*b* (Fig. S2, ESI†) shows that both synthetic routes give similar spectra, and the bands observed fit with those for Bi–S and Bi–Bi for the BiSI and $Bi_{13}S_{18}I_2$ phases.

Thermogravimetric analysis (TGA) was carried out to confirm the purity of prepared BiSI and $Bi_{13}S_{18}I_2$ samples. The TGA data collected on heating BiSI-*b* and $Bi_{13}S_{18}I_2$-*b* samples to 800 °C under a nitrogen gas flow, are presented in Fig. 5 and their DSC–TGA data are shown in Fig. S3 (ESI†). The TGA data collected on BiSI show that the decomposition has three distinct stages; the first stage is between 370 °C and 440 °C, the second stage is between 440 °C and 595 °C and the third stage occurs above 595 °C. The decomposition of $Bi_{13}S_{18}I_2$ has two stages which are consistent with the second and third decomposition stages of BiSI. To monitor the decomposition processes and determine the phases that form on heating both of these materials, PXRD data were collected on separate samples that were heated to 440 °C and 600 °C, which were found to be temperatures where weight loss events occurred during the TGA experiments. The results from analysis of the PXRD data collected on samples from the *ex situ* heating experiments show that at 440 °C, BiSI has transformed to $Bi_{13}S_{18}I_2$ and its PXRD pattern is shown in Fig. S4 (ESI†). When $Bi_{13}S_{18}I_2$ was heated to 600 °C, it decomposes to Bi_2S_3, which also requires a redox reaction to convert Bi^{2+} to Bi^{3+}. This disproportionation reaction produced Bi and Bi_2S_3 and BiI_3. PXRD data which were collected at 600 °C are shown in Fig. S4 (ESI†), indicating that Bi_2S_3 and Bi were formed. After heating to 800 °C and cooling to room temperature, only small white metallic balls remained. The decomposition reactions of the three stages are:

$$36BiSI(s) \rightarrow 2Bi_{13}S_{18}I_2(s) + 10BiI_3(g) + I_2(g) \quad (1)$$

$$3Bi_{13}S_{18}I_2(s) \rightarrow 18Bi_2S_3(s) + 2BiI_3(g) + Bi(l) \quad (2)$$

$$Bi_2S_3(s) \rightarrow 2Bi(l) + 3S(g) \quad (3)$$

This journal is © The Royal Society of Chemistry 2020

J. Mater. Chem. C, 2020, **8**, 13253–13262 | **13255**
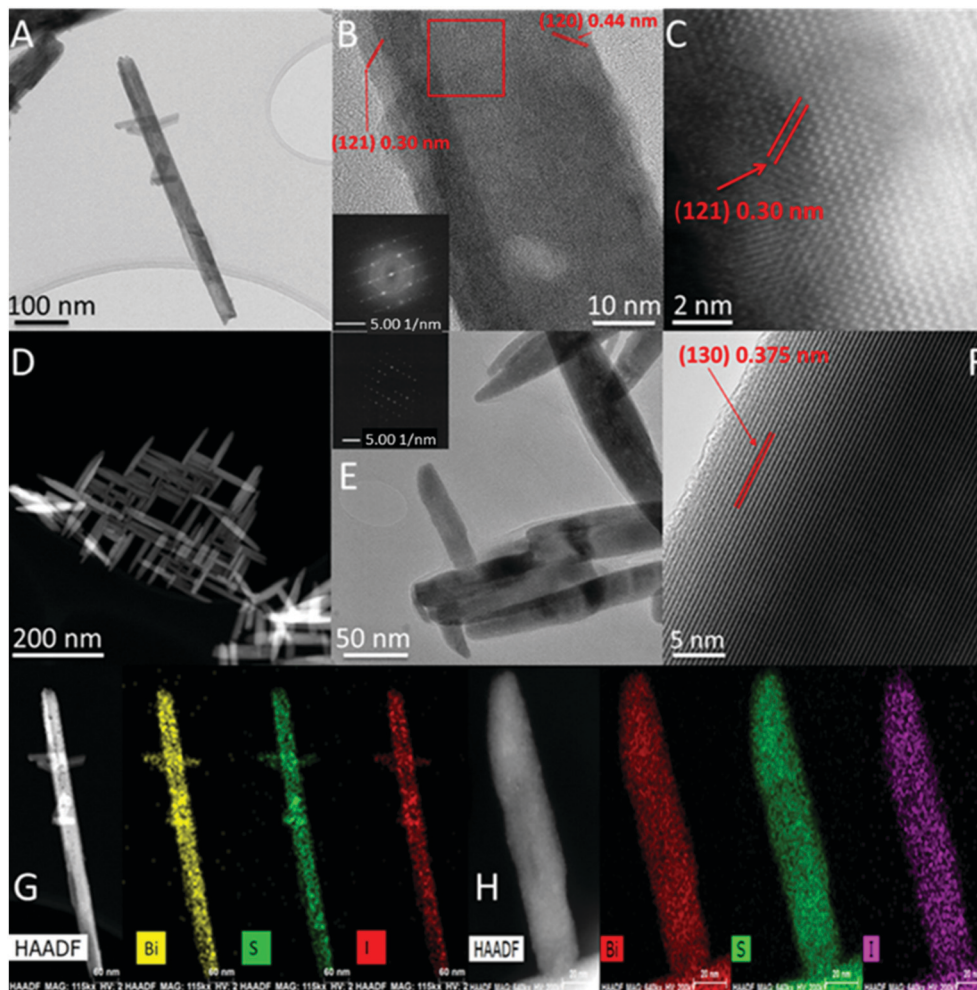
Fig. 3 TEM images of BiSI-*b* (A and B) and Bi$_{13}$S$_{18}$I$_2$-*b* (D and E) and HRTEM images of BiSI-*b* and B$_{i13}$S$_{18}$I$_2$-*b* (C from the red square of image B and F from the red square of image E), with their corresponding elemental maps BiSI-*b* (G) and B$_{i13}$S$_{18}$I$_2$-*b* (H) respectively.
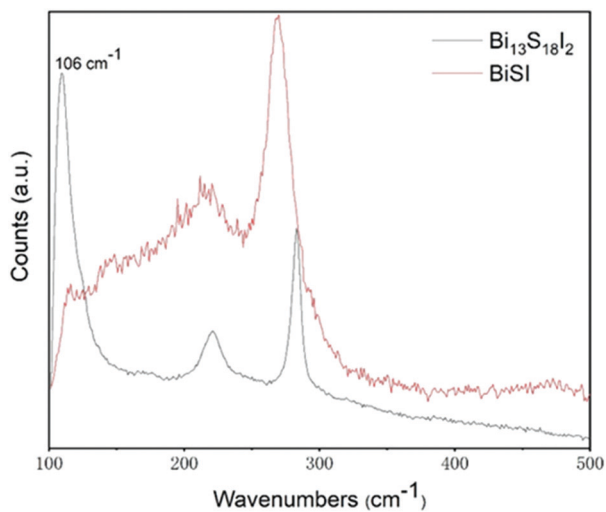

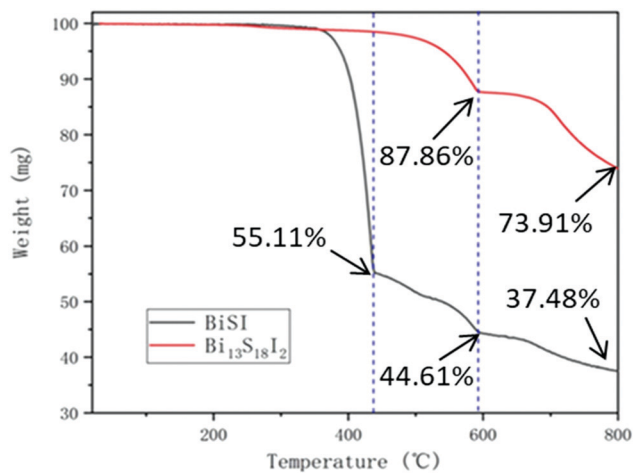**Fig. 4** Raman spectra of BiSI-*b* and Bi$_{13}$S$_{18}$I$_2$-*b*.

Fig. 5 TGA data collected on BiSI-*b* and Bi1$_3$S$_{18}$I$_2$-*b* under a Nitrogen gas flow.

The experimental weight loss values and the theoretical weight loss values, calculated from the above three equations, are shown in Table S1 (ESI†). It can be seen that the experimental weight loss values are consistent with the theoretical calculated values, which confirms the decomposition steps outlined above.

Fig. 6 presents the X-ray photoelectron spectra (XPS) of BiSI and $Bi_{13}S_{18}I_2$ powders. Comparing the Bi 4f orbital bonding energy of $Bi_{13}S_{18}I_2$ with BiSI, the values are shifted to lower energy, whereas the bonding energy of S 2s is shifted to higher energy from 225.83 eV to 227.31 eV. Table S2 (ESI†) tabulates the observed experimental atomic percentages of specific bismuth, iodine, and sulfur in the powder and the values agree closely with the theoretical atomic composition of BiSI and $Bi_{13}S_{18}I_2$. This indicates high purity BiSI and $Bi_{13}S_{18}I_2$ materials have been synthesized.
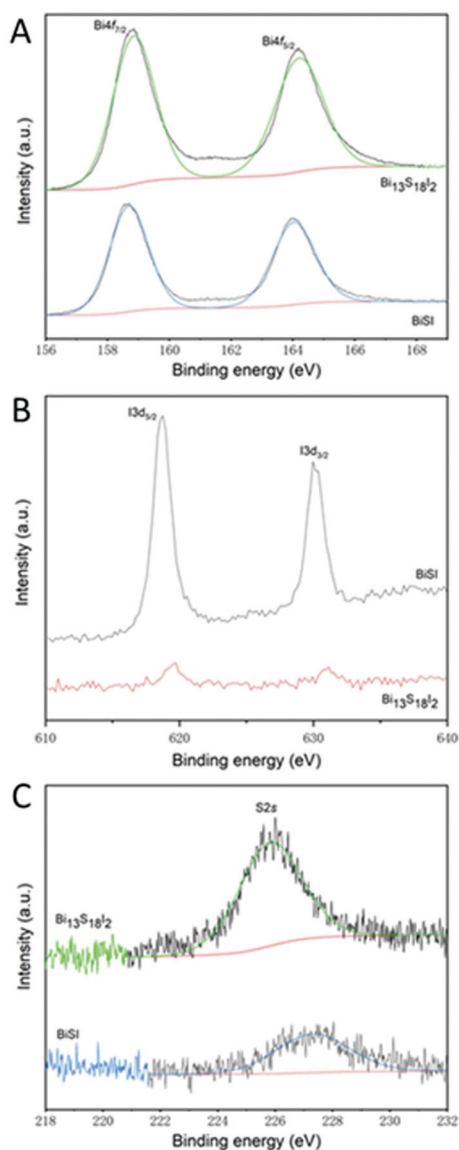

Fig. 6 High resolution X-ray photoelectron spectrum of Bi 4f (A), S 2p (B) and I 3d (C) for BiSI-*b* and $Bi_{13}S_{18}I_2$-*b* powder; specific peaks are labelled.

Typical nitrogen adsorption–desorption isotherms for BiSI and $Bi_{13}S_{18}I_2$ powder are shown in Fig. 7. After analysis based on the Brunauer–Emmett–Teller (BET) equation:[34]

$$\frac{1}{V[(P_0/P) - 1]} = \frac{1}{V_m c} + \frac{1}{V_m c (P/P_0)}$$

where P and P_0 are the equilibrium and the saturation pressure of the adsorption at the temperature of adsorption, V is the adsorbed gas quantity, V_m is the maximum monolayer adsorption quantity, c is the BET constant, the specific surface areas for BiSI-*a*, BiSI-*b*, $Bi_{13}S_{18}I_2$-*a* and $Bi_{13}S_{18}I_2$-*b* are calculated as 5.21 m² g⁻¹, 5.86 m² g⁻¹, 12.27 m² g⁻¹ and 14.98 m² g⁻¹ respectively. It can be seen from Fig. 7 that both BiSI-*b* and $Bi_{13}S_{18}I_2$-*b* have smaller pore size than BiSI-*a* and $Bi_{13}S_{18}I_2$-*a*, which indicates our novel synthetic route has increased the surface area and reduced the pore size of BiSI and $Bi_{13}S_{18}I_2$ samples compared with the autoclave route. The $Bi_{13}S_{18}I_2$-*b* sample has an average pore diameter of around 17 nm in the range of 2–50 nm which is considered as the ideal structure as EDLC electrodes.[35]

The BiSI and $Bi_{13}S_{18}I_2$ samples were first tested as electrode materials for supercapacitors using a three-electrode system at room temperature, which is appropriate to give an overview of processes at different potentials. Fig. 8A and C show a series of CV profiles measuring the BiSI-*b* sample over a potential window of −1.0 to 0 V *vs.* Ag/AgCl with scan rates from 10 to 100 mV s⁻¹. At more negative potentials, the CV profiles are different to the conventional rectangles for EDLC, suggesting pseudo-capacitive features. CV profiles consist of one reduction peak and two oxidation zones. In detail, for the case of low scan rate of 10 mV s⁻¹, the reduction peak (R1) is located at −1 V, which is caused by the reduction of Bi^{3+} to Bi; furthermore, there are two oxidation peaks; O1 at −0.62 V and O2 at −0.42 V. These can be assigned to the oxidation process of $Bi^{\circ} \rightarrow Bi^+$ and $Bi^+ \rightarrow Bi^{3+}$, respectively.[36,37] With increasing scan rate, the CV curve of sample BiSI-*b* shows oxidation peaks shifting to a more positive potential while reduction peaks shift to a more negative potential, as shown in Fig. 8A. This phenomenon is very common for CV curves, mainly derived from their iR drops or ion diffusion.[38]

Fig. 8B displays overall galvanostatic charge–discharge (GCD) profiles of the BiSI-*b* sample at various current densities, between 2 and ~10 A g⁻¹, while designating a potential
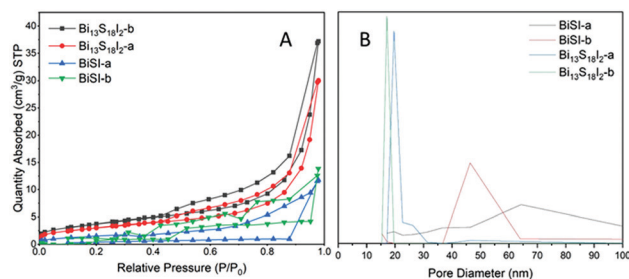

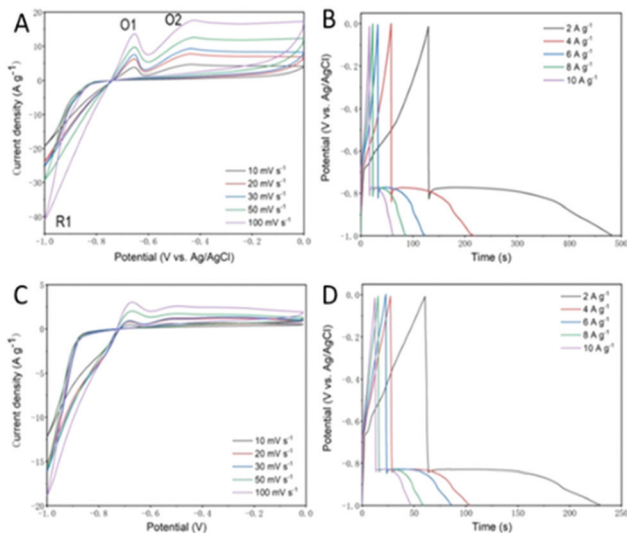**Fig. 7** Nitrogen adsorption–desorption isotherms (A) and pore size distribution (B) for BiSI and $Bi_{13}S_{18}I_2$ powder.

Fig. 8 Cyclic voltammograms collected at different scan rates for BiSI-*b* and Bi$_{13}$S$_{18}$I$_2$-*b* electrode (A and C) and their charge–discharge curves at various current densities (B and D).
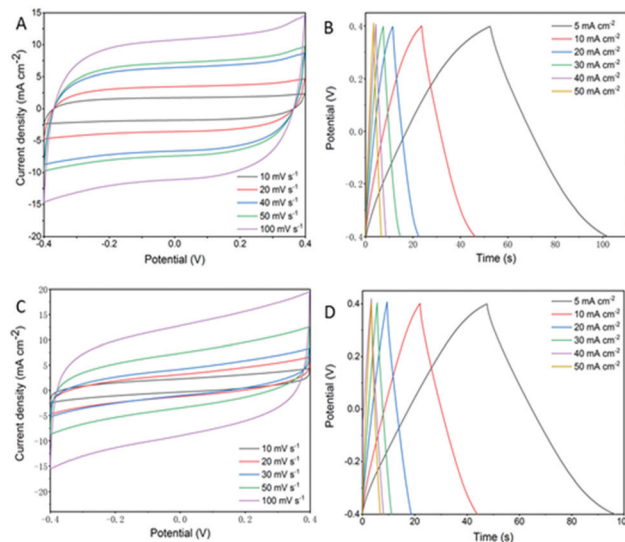

Fig. 9 Cyclic voltammograms collected at different scan rates for BiSI-*b* and Bi$_{13}$S$_{18}$I$_2$-*b* electrode as EDLC (A and C) and their charge–discharge curves at various current densities (B and D).

window of −1.0 to ∼0 V. GCD profiles present unique charging–discharging features, with asymmetric curves differing from typical triangular outlines, which indicate pseudo-capacitive characteristics. For the dis-charging stage, there are two quite distinct processes including a steep voltage drop and gradual voltage drop. The former steep voltage drop is very different to the triangular outline, probably due to the internal resistance, while the latter originated from the involvement of a quasi-faradaic process in the sample. Other kinds of bismuth-based compounds, such as Bi$_2$O$_3$[14] and SWCNT/BiVO$_4$[39] composites, are also reported to exhibit approximate pseudo-capacitive GCD behaviour. The specific capacitances were also calculated from the slope of the discharge curves according to:[40]

$$C_{\text{specific}}[=] \ (\text{F g}^{-1}) = \frac{i}{\dfrac{\text{d}V}{\text{d}t} \times m}$$

$$C_{\text{areal}}[=] \ (\text{F cm}^{-2}) = \frac{i}{\dfrac{\text{d}V}{\text{d}t} \times \text{Area}}$$

where *i* is the constant current (A), d*V*/d*t* is the slope of the discharge curve taken in the voltage range 0–1 V for consistency, area is the average geometric area of the two electrodes (cm^2) and *m* is combined mass of the active material on the working electrode (g). The specific capacitances of the BiSI-*b* electrode were 128 F g^{-1}, 121 F g^{-1}, 106 F g^{-1}, 100 F g^{-1} and 90 F g^{-1} with increasing current densities from 2 A g^{-1} to 10 A g^{-1}, which suggests that the specific capacitance of the electrode decreases with increase in current density. The specific capacitances of the Bi$_{13}$S$_{18}$I$_2$-*b* electrode were 86 F g^{-1}, 78 F g^{-1}, 76 F g^{-1}, 72 F g^{-1} and 59 F g^{-1} with increasing current densities from 2 A g^{-1} to 10 A g^{-1}.

To further investigate the electrochemical performance, the prepared BiSI and Bi$_{13}$S$_{18}$I$_2$ samples were tested under a two-electrode system at room temperature, which is the configuration of an actual supercapacitor device. As shown in Fig. 9, the CV and GCD curves measured in the two-electrode system showed significant changes in shape compared with those achieved in the three-electrode system (Fig. 8), and the CV showed significant rectangular features. This is due to the controlled voltage range such that we are no longer scanning into the range where faradaic processes occur. GCD shows a distinct triangle, which is a feature of EDLC, free of faradaic processes that generally lead to poor stability. The area and specific capacitance of the device were calculated. When the scan rate was increased from 0.01 V s^{-1} to 0.1 V s^{-1}, the capacitance of the electrode was reduced. The reduction in capacitance is a common feature of EDLC, which is caused by different time states of charge transport and ion diffusion at different scan rates. At lower scan rates, the electrolytic ions have enough time to diffuse into the pores in the active material layer, increasing charge build up and increasing capacitance. At higher scan rates, charge accumulation is limited to the electrode surface, reducing the capacitance of the electrode.

The galvanostatic charge–discharge measurements were carried out over a −0.4 to 0.4 V window, with current densities varying from 5 mA cm^{-2} to 50 mA cm^{-2} (Fig. 9B and D). The charge–discharge curves of Bi$_{13}$S$_{18}$I$_2$-*b* and BiSI-*b* electrodes are largely symmetric and the discharge curve displays remarkable linearity following an initial iR drop even at the lowest current densities, corroborating the non-faradaic EDLC behaviour. The areal capacitances of the BiSI-*b* device were from 168 mF cm^{-2} to 99 mF cm^{-2}, and the specific capacitances of the Bi$_{13}$S$_{18}$I$_2$-*b* device were 247 mF cm^{-2} to 202 mF cm^{-2} with increasing current densities from 5 mA cm^{-2} to 50 mA cm^{-2}. The energy density and power density calculated from galvanostatic charge and discharge measurements are summarized in
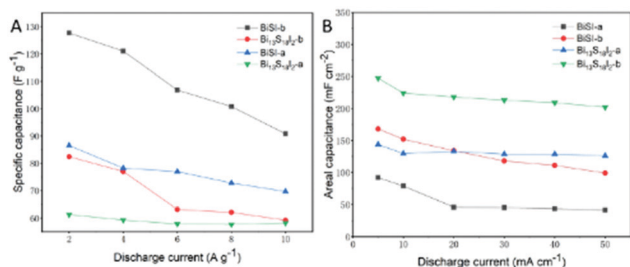
13258 | *J. Mater. Chem. C*, 2020, **8**, 13253–13262

This journal is © The Royal Society of Chemistry 2020

Fig. 10 Variation of specific capacitance of BiSI-*a*, BiSI-*b*, $Bi_{13}S_{18}I_2$-*a* and $Bi_{13}S_{18}I_2$-*b* electrodes at different discharge current density in pseudo-capacitor system (A) and EDLC system (B).

Fig. 11 PXRD patterns of (blue) as-prepared BiSI-*b* and $Bi_{13}S_{18}I_2$-*b* electrode on carbon paper and the electrodes after 2000 cycles (in three electrodes) and 5000 cycles (in two electrodes) stability test. Standard BiSI: ICDD PDF card no. 45-652 and $Bi_{13}S_{18}I_2$: ICDD PDF card no. 73-1157.

Table S3 (ESI†), which shows that the BiSI-*b* electrode has a calculated energy density of 22.2 W h kg^{-1} with a high power density of 3.15 kW kg^{-1} as a pseudo-capacitor, and the $Bi_{13}S_{18}I_2$-*b* electrode shows a calculated energy density of 2.7 W h kg^{-1} with a high power density of 3.98 kW kg^{-1} as EDLC.

The comparison of specific capacitance of four BiSI and $Bi_{13}S_{18}I_2$ electrodes in pseudo-capacitor system is shown in Fig. 10A and areal capacitance in EDLC system is shown in Fig. 10B at different discharge current density. Fig. 10B shows that compared with BiSI electrodes, both samples of $Bi_{13}S_{18}I_2$ prepared as electrodes have much larger areal capacitance and better capacitance retention with increased discharge current density, especially so for sample $Bi_{13}S_{18}I_2$-*b*. Electrochemical performance is affected by the electrode morphology and the size of the active material. Nanoparticles of about 20 nm can increase the capacitance of EDLC.[41] From the SEM image, we have shown that $Bi_{13}S_{18}I_2$-*b* particles have the smallest size of around 40 nm, which can effectively shorten the nanoscale electron diffusion length during the charge and discharge process. This will improve the electrochemical utilization rate, the interface contact and reduce the internal resistance. At the same time, the large surface area is beneficial to increase the capacitance of the EDLC. $Bi_{13}S_{18}I_2$-*b* has the largest surface area of the four electrodes tested here, which may be another important factor to improve its capacitance. Comparing the two synthetic routes, the capacitance of the two samples (BiSI-*a* and $Bi_{13}S_{18}I_2$-*a*) synthesized by a hydrothermal method at 160 °C is smaller than the same component yielded by our facile solution reaction route at 120 °C.

The long term cyclic stability of a series of BiSI and $Bi_{13}S_{18}I_2$ EDLC electrodes was measured by the galvanostatic charge/discharge technique at a constant current density of 10 A g^{-1} over 5000 cycles, and the data are shown in Fig. S6 (ESI†). The specific capacitance of four electrodes all remained over 98% of the initial capacitance after 5000 cycles, which indicated they have remarkable cycle stability at high current conditions over long charge/discharge processes, especially for the $Bi_{13}S_{18}I_2$-*a* sample, which retained 99.2% of its initial capacitance. The PXRD patterns of the BiSI-*b* and $Bi_{13}S_{18}I_2$-*b* electrodes before and after 5000 charge/discharge cycles as EDLC using two electrodes (2E) and pseudo-capacitor using three electrodes (3E) are compared in Fig. 11, and other electrodes are shown
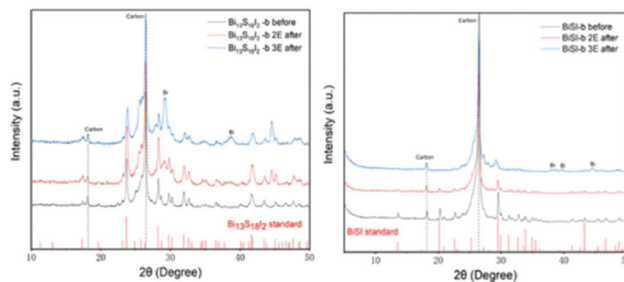
in Fig. S6 (ESI†). It can be clearly seen that the PXRD patterns of both BiSI and $Bi_{13}S_{18}I_2$ electrode as EDLC (2E) have not significantly changed after 5000 cycles, indicating much of the starting bismuth sulfide iodide materials remain, especially for the $Bi_{13}S_{18}I_2$-*b* sample. However, the PXRD patterns of the electrodes, when operated as a pseudo-capacitor (3E) by using a larger voltage range, shows that most of the BiSI and $Bi_{13}S_{18}I_2$ peaks have disappeared and new peaks are observed due to the formation of Bi during a faradaic reaction. SEM images of $Bi_{13}S_{18}I_2$-*b* electrode after undergoing the 5000 cycles as EDLC indicate that the surface coverage of the carbon paper with the activated $Bi_{13}S_{18}I_2$ remained largely the same after cycling (Fig. S7, ESI†). Moreover, the EDS results in Fig. S7 (ESI†) of three points on the electrode after 5000 EDLC cycles, show that the elemental composition of the active material on the electrode surface is basically the same as before the cycling. This proves that there is no chemical reaction process during the charge/discharge cycle, resulting in its excellent capacitance retention. This is consistent with the results from analysis of PXRD data and SEM images on the $Bi_{13}S_{18}I_2$ material after 5000 cycles. Conversely, the SEM image of electrodes after 2000 pseudo-capacitor cycles (Fig. S7, ESI†) shows that the ~1 μm length needle-like $Bi_{13}S_{18}I_2$ structure has disappeared and has been replaced by nanoparticles of around 300 nm. Further EDS results (Fig. S7, ESI†) shows that the peaks relating to the presence of S and I disappear, with only the peaks relating to the presence of Bi remaining. This is consistent with the results from analysis of PXRD data and SEM images and is explained by the significant decrease of stability caused by the irreversible faradaic reaction in the pseudo-capacitor system.

Electrochemical impedance spectroscopy (EIS) was carried out in the three-electrode test system to characterize the physical and electrochemical processes of the BiSI and $Bi_{13}S_{18}I_2$ electrodes as supercapacitors in response to AC currents at different frequencies. All EIS measurements were conducted at their open circuit potential with an AC amplitude of 10 mV at a frequency of 150 kHz to 0.1 Hz. The Nyquist plot of the BiSI and $Bi_{13}S_{18}I_2$ electrodes both show a typical faradaic pseudocapacitance behavior with a semicircle in the high frequency region, and a line towards vertical in the low frequency region in Fig. 12A, which is close to a mixture of typical battery
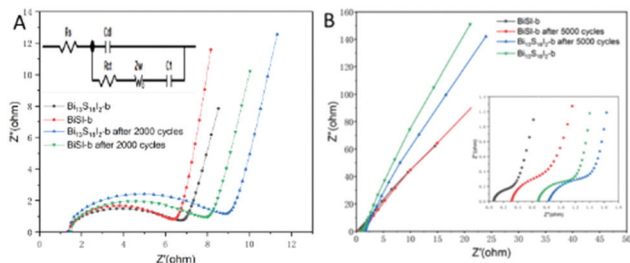
This journal is © The Royal Society of Chemistry 2020

J. Mater. Chem. C, 2020, **8**, 13253–13262 | **13259**

Fig. 12 Experimental Nyquist plots of BiSI-*b* and $Bi_{13}S_{18}I_2$-*b* electrodes before and after 2000 cycles in tree electrodes system (A) and after 5000 cycles in EDLC system (B), with equivalent circuit inserted.

characteristic and capacitor behaviour.[42] The intercept of the semicircle at the high frequency end of the real axis (Z') gives the value of R_s in the equivalent circuit, indicating the combined resistance due to the resistance in the KOH electrolyte and the current collector. This is usually referred to as the equivalent series resistance (ESR). Since all charge transfer during charge–discharge occurs through the electrolyte, R_s is connected in series with other circuit components and found to be approximately 1.24 Ω to 1.52 Ω. The diameter of the semicircle and curvature are simulated with resistor R_{ct} in parallel with a constant phase element C_{dl} to indicate two possible behaviors of the electrolyte during charging and discharging. At moderate frequencies, the ions penetrate the active layer of the electrodes, introducing R_{ct} with a calculated value of 3.01 Ω ($Bi_{13}S_{18}I_2$-*b*), 3.22 Ω (BiSI-*b*), 3.52 Ω ($Bi_{13}S_{18}I_2$-*b* after 2000 cycles) and 3.94 Ω (BiSI-*b* after 2000 cycles), which was analysed based on the diameter of semicircle, representing the charge transfer resistance and the bulk resistance of the active material and electrode pores. The R_{ct} of $Bi_{13}S_{18}I_2$ electrode is smaller than the BiSI electrode, which may be due to the smaller particle size of $Bi_{13}S_{18}I_2$ leading to smaller bulk resistance. At lower frequencies, the ions can diffuse into the narrow pores of the porous electrode and the slope of the line represents diffuse layer resistance including double layer formation and ion diffusion process. Nyquist plots of the BiSI and $Bi_{13}S_{18}I_2$ electrodes both show typical EDLC behaviour in EDLC test system with quasi-vertical line in Fig. 12B.[43–45] It can be seen from the enlarged image of high frequency area in Fig. 12B that both BiSI-*b* and $Bi_{13}S_{18}I_2$-*b* have a very small semicircle and its diameter is assigned to the electrolyte resistance in the pores of the electrodes.[46] After 5000 cycles, the Nyquist plot of both BiSI-*b* and $Bi_{13}S_{18}I_2$-*b* are basically the same as before the cycles, indicating good cycle stability. The electrolyte resistance in the pores of the electrodes slightly increased after cycles. This may be because the electrolyte enters the lattice of the electrode material during the cycling process, which reduces the conductivity of the electrode material in the pore of the electrodes.

Conclusions

We have demonstrated the first low-temperature, and solution-based synthesis of the bismuth chalcogenide materials, BiSI

and $Bi_{13}S_{18}I_2$. We systematically studied the effect of reaction temperature and time on the reaction product and found the optimum reaction conditions for the synthesis of pure BiSI and $Bi_{13}S_{18}I_2$ powders is at 120 °C for one hour. We have characterized the electrodes to show the potential range of both faradaic pseudo-capacitances and non-faradaic EDLC behaviour using a mass load (4–5 mg cm^{-2}) of BiSI and $Bi_{13}S_{18}I_2$ active materials and 3 M KOH as the electrolyte. In two-electrode devices, all BiSI and $Bi_{13}B_{18}I_2$ EDLCs have excellent capacitance retention, especially the $Bi_{13}B_{18}I_2$ capacitor, which has a capacitance of 247 mF cm^{-2} at the current density of 5 mA cm^{-2} and an excellent capacitance retention of 98.4% after 5000 cycles. Furthermore, all samples formed using our straightforward, ambient-pressure synthetic route have higher specific surface area and higher specific capacitance than the samples using a hydrothermal route at high pressure. For the first time, we have shown that BiSI and $Bi_{13}S_{18}I_2$ materials can be integrated into low-cost promising energy storage devices with excellent long-term cycle stability and we have removed the need for high pressure and high temperature to synthesise BiSI and $Bi_{13}S_{18}I_2$, making large-scale industrial production possible. In addition, this new synthesis route allows much further optimization to be carried out through blending these bismuth chalcogenide materials with other materials, optimizing the electrolyte and making asymmetric supercapacitors to further enhance the performance.

Experimental

Synthesis and characterization

All reagents were obtained from commercial suppliers (Acros Organics, Sigma Aldrich, Fluka) and used as received unless otherwise stated. Solvents used were of analytical grade (Sigma Aldrich, Fisher Scientific, VWR Chemicals, and Cambridge Isotope Laboratories).

Two different routes were used to synthesize BiSI. First, 4.4 g (58 mmol) thiourea and 5.1 g (20 mmol) I_2 were mixed and ground in a mortar and pestle for 20 minutes. This powder mixture and 9.7 g (20 mmol) $Bi(NO_3)_3 \cdot 5H_2O$ were transferred to a 100 mL Teflon-lined autoclave with 60 mL deionized water. The autoclave was heated to 160 °C for 15 hours and was then cooled to room temperature. The final product was washed and centrifuged several times with ethanol and deionized water until the liquid became clear. The precipitate was dried in an oven at 70 °C for 8 hours. The product of this route will be known as BiSI-*a* with a yield of 71%. The second route is to dissolve 0.485 g (1.0 mmol) $Bi(NO_3)_3 \cdot 5H_2O$ in 20 mL deionized water and heat to 120 °C. This solution was slowly added to a mixture of 0.17 g (1.0 mmol) KI and 0.2 g (2.7 mmol) thioacetamide (TAA) in 20 mL deionized water which was already heated to 120 °C. The pH value of the solution was adjusted to 1 by acetic acid. After heating for 1 hour at 120 °C, the precipitate was washed and dried using the same process as the first route and the final product will be known as BiSI-*b* with a yield of 82%.

Two different synthetic routes were also employed to synthesize $Bi_{13}S_{18}I_2$. First, 1.27 g (0.5 mmol) I_2 were ground for

5 minutes. This I_2 powder, 4.56 g (0.06 mmol) thiourea and 9.7 g (2.0 mmol) $Bi(NO_3)_3 \cdot 5H_2O$ were transferred to a 100 mL Teflon-lined autoclave with 40 mL deionized water. The autoclave was heated to 160 °C for 15 hours and then cooled to room temperature. The final product was washed and centrifuged several times with ethanol and DI water until the liquid became clear. The precipitate was dried in an oven at 70 °C for 8 hours and will be known as $Bi_{13}S_{18}I_2$-*a* with a yield of 68%. The second route for synthesis of $Bi_{13}S_{18}I_2$ was to dissolve 0.485 g (1.0 mmol) $Bi(NO_3)_3 \cdot 5H_2O$ in 20 mL DI water to form a suspension and heated to 120 °C. The suspension was slowly added to a mixture of 0.03 g (0.18 mmol) KI and 0.2 g (2.7 mmol) thioacetamide (TAA) in 20 mL deionized water in a 100 mL beaker which was already heated to 120 °C. The pH of the solution was adjusted to 1 by acetic acid. After heating the solution for 1 hour at 120 °C, the precipitate formed was washed and dried using the same process as the first route and the final product was marked as $Bi_{13}S_{18}I_2$-*b* with a yield of 77%.

Powder X-ray diffraction (PXRD) data were collected using a Bruker (D2 Advance) diffractometer with Cu-Kα radiation (λ = 1.5418 Å), at room temperature over a 2-theta range of 5° to 60°, with a stepsize of 0.1° and a count time of 0.45 s per step. X-ray photoelectron spectra were acquired using a Thermo Scientific (VG Sigma Probe) XPS spectrometer with monochromatic Al-Kα as the source of X-rays. Scanning electron microscopy was carried out using a Zeiss (SIGMA HD VP) Field Emission-Scanning Electron Microscope (SEM) operating with an accelerating voltage of 10 kV. Transmission Electron Microscopy (TEM) and Electron Dispersive Spectroscopy (EDS) were carried using a FEI Titan Themis microscope operating with an accelerating voltage of 200 kV. Nitrogen adsorption experiments were carried out to determine specific surface areas of the samples using a JWGB SCI. & TECH BK132F automatic adsorption instrument. Raman spectra were acquired using a Renishaw in *Via* Raman Microscope with an excitation laser wavelength of 785 nm and a spectral resolution of approximately 1 cm^{-1}. The TGA–DSC experiments were carried out using a TA Instruments SDT Q600, samples were heated from room temperature to 800 °C under flowing Nitrogen with a ramp rate of 10 degree per minute.

Measurement of electrochemical properties

The working electrodes for both the three electrodes system and two-electrode EDLC system were prepared by mixing BiSI and $Bi_{13}S_{18}I_2$ powder with activated charcoal powder and PTFE powder in 1 mL ethanol as the solvent to make a final $Bi_{13}S_{18}I_2$: charcoal : PTFE mixture with a weight ratio of 85 : 10 : 5. The resulting suspended solution was sonicated until homogenized, and around 200 μL was drop-coated onto 1 cm^2 conductive carbon paper (ELAT, NuVant Systems Inc.) substrate and dried at 90 °C for 6 hours. The active mass of deposited BiSI-*a*, BiSI-*b*, $Bi_{13}S_{18}I_2$-*a* and $Bi_{13}S_{18}I_2$-*b* electrodes were 4.4 mg, 4.0 mg, 4.5 mg and 4.4 mg, respectively, used for all subsequent calculations. When assembling the EDLC, two coated electrodes were separated by a thin polymer separator (Celgard 3501) pre-soaked in a 3.0 M KOH aqueous electrolyte solution and then sandwiched in a symmetrically-assembled capacitor test cell (ECC-std, EL-CELL GmbH). In the three-electrode system, Ag/AgCl (3.0 M KCl) and a Pt wire were used as the reference and counter electrode, respectively with 3.0 M KOH aqueous electrolyte. Cyclic voltammetry (CV), galvanostatic charge/discharge measurements and electrochemical impedance spectroscopy (EIS) were carried out using an Autolab electrochemical work station with FRA2 module using General Purpose Electrochemical System (GPES) and Frequency Response Analyser (FRA) software.

Conflicts of interest

The authors state there are no conflicts to declare.

Acknowledgements

Notes and references

1 C. Guan, X. Liu, W. Ren, X. Li, C. Cheng and J. Wang, *Adv. Energy Mater.*, 2017, **7**, 1602391.

2 M. Hannan, M. Hoque, A. Mohamed and A. Ayob, *Renewable Sustainable Energy Rev.*, 2017, **69**, 771–789.

3 M. B. Tayel, M. M. Soliman, S. Ebrahim and M. E. Harb, *J. Electron. Mater.*, 2016, **45**, 820–828.

4 J. Zhou, H. Zhao, X. Mu, J. Chen, P. Zhang, Y. Wang, Y. He, Z. Zhang, X. Pan and E. Xie, *Nanoscale*, 2015, **7**, 14697–14706.

5 L. Feng, Y. Zhu, H. Ding and C. Ni, *J. Power Sources*, 2014, **267**, 430–444.

6 M. M. Sk, C. Y. Yue, K. Ghosh and R. K. Jena, *J. Power Sources*, 2016, **308**, 121–140.

7 J. Xu, Y. Li, L. Wang, Q. Cai, Q. Li, B. Gao, X. Zhang, K. Huo and P. K. Chu, *Nanoscale*, 2016, **8**, 16761–16768.

8 S. Goriparti, E. Miele, F. De Angelis, E. Di Fabrizio, R. P. Zaccaria and C. Capiglia, *J. Power Sources*, 2014, **257**, 421–443.

9 X.-Y. Hou, X.-L. Yan, X. Wang and Q.-G. Zhai, *J. Solid State Chem.*, 2018, **263**, 72–78.

10 Y. Zeng, Z. Lin, Y. Meng, Y. Wang, M. Yu, X. Lu and Y. Tong, *Adv. Mater.*, 2016, **28**, 9188–9195.

11 F.-L. Zheng, G.-R. Li, Y.-N. Ou, Z.-L. Wang, C.-Y. Su and Y.-X. Tong, *Chem. Commun.*, 2010, **46**, 5021–5023.

12 Y. Qiu, H. Fan, X. Chang, H. Dang, Q. Luo and Z. Cheng, *Appl. Surf. Sci.*, 2018, **434**, 16–20.

13 Y. Qiu, D. Liu, J. Yang and S. Yang, *Adv. Mater.*, 2006, **18**, 2604–2608.

14 Y. Qiu, M. Yang, H. Fan, Y. Zuo, Y. Shao, Y. Xu, X. Yang and S. Yang, *CrystEngComm*, 2011, **13**, 1843–1850.

This journal is © The Royal Society of Chemistry 2020

J. Mater. Chem. C, 2020, **8**, 13253–13262 | **13261**

15 S. Wang, C. Jin and W. Qian, *J. Alloys Compd.*, 2014, **615**, 12–17.

16 M. Ciszewski, A. Mianowski, P. Szatkowski, G. Nawrat and J. Adamek, *Ionics*, 2015, **21**, 557–563.

17 X. Yang, S. Tian, R. Li, W. Wang and S. Zhou, *Sens. Actuators, B*, 2017, **241**, 210–216.

18 T. Liu, Y. Zhao, L. Gao and J. Ni, *Sci. Rep.*, 2015, **5**, 9307.

19 X. Yu, J. Zhou, Q. Li, W.-N. Zhao, S. Zhao, H.-M. Chen, K. Tao and L. Han, *Dalton Trans.*, 2019, **48**, 9057–9061.

20 W. Luo, F. Li, Q. Li, X. Wang, W. Yang, L. Zhou and L. Mai, *ACS Appl. Mater. Interfaces*, 2018, **10**, 7201–7207.

21 R. Groom, A. Jacobs, M. Cepeda, R. Drummey and S. E. Latturner, *Chem. Mater.*, 2017, **29**, 3314–3323.

22 R. A. Groom, A. Jacobs, M. Cepeda, R. Drummey and S. E. Latturner, *Inorg. Chem.*, 2017, **56**, 12362–12368.

23 Z. S. Aliev, S. S. Musayeva, F. Y. Jafarli, I. R. Amiraslanov, A. V. Shevelkov and M. B. Babanly, *J. Alloys Compd.*, 2014, **610**, 522–528.

24 C.-H. Ho, Y.-H. Chen, Y.-K. Kuo and C. Liu, *Chem. Commun.*, 2017, **53**, 3741–3744.

25 B. Xu, T. Feng, M. T. Agne, Q. Tan, Z. Li, K. Imasato, L. Zhou, J. H. Bahk, X. Ruan and G. J. Snyder, *Angew. Chem.*, 2018, **130**, 2437–2442.

26 Y. Yan, Y. Xu, S. Lei, X. Ou, L. Chen, J. Xiong, Y. Xiao and B. Cheng, *Dalton Trans.*, 2018, **47**, 3408–3416.

27 S. Li, L. Xu, X. Kong, T. Kusunose, N. Tsurumachi and Q. Feng, *J. Mater. Chem. C*, 2020, **8**, 3821–3829.

28 K. Adams, A. F. González, J. Mallows, T. Li, J. H. Thijssen and N. Robertson, *J. Mater. Chem. A*, 2019, **7**, 1638–1646.

29 W. Hasse-Wessel, *Naturwissenschaften*, 1973, **60**, 474.

30 G. Miehe and V. Kupčík, *Naturwissenschaften*, 1971, **58**, 219.

31 R. Zou, Z. Zhang, M. F. Yuen, M. Sun, J. Hu, C.-S. Lee and W. Zhang, *NPG Asia Mater.*, 2015, **7**, e195.

32 Z. Sun, S. Firdoz, E. Y.-X. Yap, L. Li and X. Lu, *Nanoscale*, 2013, **5**, 4379–4387.

33 H. Kalpen, W. Hoenle, M. Somer, U. Schwarz, K. Peters, H. von Schnerig and R. J. C. Blachnik, *J. Cheminf.*, 1998, **29**, 1137–1147.

34 S. Brunauer, P. H. Emmett and E. Teller, *J. Am. Chem. Soc.*, 1938, **60**, 309–319.

35 A. Fuertes, G. Lota, T. Centeno and E. Frackowiak, *Electrochim. Acta*, 2005, **50**, 2799–2805.

36 B. Sarma, A. L. Jurovitzki, Y. R. Smith, S. K. Mohanty and M. Misra, *ACS Appl. Mater. Interfaces*, 2013, **5**, 1688–1697.

37 V. Vivier, A. Regis, G. Sagon, J.-Y. Nedelec, L. Yu and C. Cachet-Vivier, *Electrochim. Acta*, 2001, **46**, 907–914.

38 Y. Arora, A. P. Shah, S. Battu, C. B. Maliakkal, S. Haram, A. Bhattacharya and D. Khushalani, *Sci. Rep.*, 2016, **6**, 36294.

39 Z. J. Zhang, Q. C. Zheng and L. Sun, *Ceram. Int.*, 2017, **43**, 16217–16224.

40 E. Barsoukov and J. R. Macdonald, *Impedance spectroscopy: theory, experiment, and applications*, John Wiley & Sons, 2018.

41 C. Portet, G. Yushin and Y. Gogotsi, *J. Electrochem. Soc.*, 2008, **155**, A531–A536.

42 S. Zhang, K. Xu and T. Jow, *Electrochim. Acta*, 2006, **51**, 1636–1640.

43 H. M. Coromina, B. Adeniran, R. Mokaya and D. A. Walsh, *J. Mater. Chem. A*, 2016, **4**, 14586–14594.

44 C. Lei, F. Markoulidis, Z. Ashitaka and C. Lekakou, *Electrochim. Acta*, 2013, **92**, 183–187.

45 I. Yang, S.-G. Kim, S. H. Kwon, M.-S. Kim and J. C. Jung, *Electrochim. Acta*, 2017, **223**, 21–30.

46 B.-A. Mei, O. Munteshari, J. Lau, B. Dunn and L. Pilon, *J. Phys. Chem. C*, 2018, **122**, 194–206.

13262 | *J. Mater. Chem. C*, 2020, **8**, 13253–13262

This journal is © The Royal Society of Chemistry 2020